

# Novel PET Probes $^{18}\text{F}$ -BCPP-EF and $^{18}\text{F}$ -BCPP-BF for Mitochondrial Complex I: A PET Study in Comparison with $^{18}\text{F}$ -BMS-747158-02 in Rat Brain

Hideo Tsukada, Shingo Nishiyama, Dai Fukumoto, Masakatsu Kanazawa, and Norihiro Harada

Central Research Laboratory, Hamamatsu Photonics K.K., Hamamatsu, Shizuoka, Japan

We developed novel PET probes, 2-*tert*-butyl-4-chloro-5-[6-[2-( $^{18}\text{F}$ -fluoroethoxy)-ethoxy]-pyridin-3-ylmethoxy]-2H-pyridazin-3-one ( $^{18}\text{F}$ -BCPP-EF) and 2-*tert*-butyl-4-chloro-5-[6-(4- $^{18}\text{F}$ -fluorobutoxy)-pyridin-3-ylmethoxy]-2H-pyridazin-3-one ( $^{18}\text{F}$ -BCPP-BF), for quantitative imaging of mitochondrial complex I (MC-I) activity in the brain and preliminarily evaluated their properties in comparison with  $^{18}\text{F}$ -BMS-747158-02 ( $^{18}\text{F}$ -BMS). **Methods:** The affinity of  $^{18}\text{F}$ -BCPP-EF,  $^{18}\text{F}$ -BCPP-BF, and  $^{18}\text{F}$ -BMS to MC-I was analyzed using in vitro binding assays with  $^3\text{H}$ -dihydrorotenone and bovine cardiomyocyte submitochondrial particles.  $^{18}\text{F}$ -BCPP-EF,  $^{18}\text{F}$ -BCPP-BF, or  $^{18}\text{F}$ -BMS was intravenously injected into rats, and the uptake (standardized uptake value) in each organ was determined by dissection method. The effects of rotenone, a specific MC-I inhibitor, on the uptake of each probe were assessed by whole-body PET imaging in rats. Ischemic brain model rats were imaged using  $^{18}\text{F}$ -BCPP-EF. **Results:** The rank order of affinity to MC-I was  $^{18}\text{F}$ -BCPP-BF >  $^{18}\text{F}$ -BMS >  $^{18}\text{F}$ -BCPP-EF. The uptake of  $^{18}\text{F}$ -BCPP-EF and  $^{18}\text{F}$ -BMS was high in the heart, intermediate in brain, and low in muscle and bone 60 min after the injection.  $^{18}\text{F}$ -BCPP-BF provided increasing bone uptake with time after the injection. The uptake of  $^{18}\text{F}$ -BCPP-EF and  $^{18}\text{F}$ -BMS into the brain and heart was significantly decreased by preadministration of rotenone; however, the reduction degree of  $^{18}\text{F}$ -BCPP-EF was more pronounced than that of  $^{18}\text{F}$ -BMS. Rotenone did not affect  $^{18}\text{F}$ -BCPP-BF uptake in either the brain or the heart.  $^{18}\text{F}$ -BCPP-EF imaged the cortical ischemic neuronal damage without any disturbance by microglial activation even on day 7 when  $^{18}\text{F}$ -FDG showed high uptake in the damaged area. **Conclusion:** The present study demonstrated that  $^{18}\text{F}$ -BCPP-EF could be a potential PET probe for quantitative imaging of MC-I activity and its ischemic damage in the living brain with PET.

**Key Words:** mitochondria complex I; brain; ischemia;  $^{18}\text{F}$ -BCPP-EF; PET

J Nucl Med 2014; 55:473–480

DOI: 10.2967/jnumed.113.125328

In normal mammalian cells, glucose is converted to pyruvate, followed by transformation into acetyl-coenzyme A by pyruvate dehydrogenase (Enzyme Commission Code [EC] 1.2.4.1) within

the mitochondria, which is subsequently fed into the tricarboxylic acid cycle, ultimately producing energy via the electron transport system and oxidative phosphorylation. Oxidative phosphorylation may account for approximately 85%–90% of the glucose used in adult humans (1–3). Mitochondrial complex I (MC-I; nicotinamide adenine dinucleotide–ubiquinone oxidoreductase, EC 1.6.5.3) is the first and largest macrocomplex of the respiratory electron transport chain and oxidative phosphorylation. In contrast, activated inflammatory cells (macrophages and microglia) (4–7) and cancer cells (3,8,9) produce lactate from glucose via lactate dehydrogenase subunit A (EC 1.1.1.27), which is known as the Warburg effect or aerobic glycolysis, showing less than 5% glucose utilization in oxidative phosphorylation and a low contribution of the electron transport system for adenosine triphosphate (ATP) production.

$^{18}\text{F}$ -FDG PET is a well-established technique for the quantitative measurement of the regional metabolic rate of glucose in the brain (10). However, this technique measures only the first part of glucose metabolism in the phosphorylation of glucose to glucose-6-phosphate by hexokinase (EC 2.7.1.1). Therefore,  $^{18}\text{F}$ -FDG is taken up into not only normal tissues but also inflammatory regions observed in the subacute phase after transient focal ischemia in rodent models (11,12). Because recent reports indicated that several neurodegenerative disorders—schizophrenia, major depression, dementia (13,14), and autism (15)—induced neuroinflammation,  $^{18}\text{F}$ -FDG may lead to underestimation of the neurodegenerative damage in these diseases.

For the quantitative neuroimaging of normal tissues without interference by neuroinflammation, we proposed to apply a specific PET probe for MC-I,  $^{18}\text{F}$ -BMS-747158-02 ( $^{18}\text{F}$ -BMS) (16), which was originally developed as a myocardial perfusion imaging agent (17,18). Because whole-body PET imaging indicated high uptake and long retention not only in heart but also in the brain (17), we hypothesized that  $^{18}\text{F}$ -BMS might be applicable for detecting neuronal damage in the living brain using PET. In fact, we demonstrated that  $^{18}\text{F}$ -BMS might be useful to detect ischemic neuronal damage at the subacute phase 7 d after ischemic insult (16), at which time markedly higher uptake of  $^{18}\text{F}$ -FDG, induced by microglial activation, was observed in the ischemic area (12,16). In parallel, we also found that  $^{18}\text{F}$ -BMS revealed relatively high nonspecific binding in the brain against the inhibition with rotenone, a specific MC-I inhibitor, in both in vitro and in vivo assessments (16). An ideal PET probe for MC-I should provide the specificity for MC-I with in vitro and in vivo assessments, an appropriate  $\log D_{7.4}$  (distribution coefficient at pH 7.4) value, relatively long stability in plasma with rapid clearance, high brain uptake, high metabolic stability in the brain, and long retention with gradual elimination from the brain (19). According

Received Apr. 29, 2013; revision accepted Nov. 6, 2013.

For correspondence contact: Hideo Tsukada, Central Research Laboratory, Hamamatsu Photonics K.K., 5000 Hirakuchi, Hamakita, Shizuoka 434-8601, Japan.

E-mail: tsukada@crl.hpk.co.jp

Published online Jan. 27, 2014.

COPYRIGHT © 2014 by the Society of Nuclear Medicine and Molecular Imaging, Inc.

to these criteria, we recently designed novel PET probes, 2-*tert*-butyl-4-chloro-5-[6-[2-(2-<sup>18</sup>F-fluoroethoxy)-ethoxy]-pyridin-3-ylmethoxy]-2H-pyridazin-3-one (<sup>18</sup>F-BCPP-EF) and 2-*tert*-butyl-4-chloro-5-[6-(4-<sup>18</sup>F-fluorobutoxy)-pyridin-3-ylmethoxy]-2H-pyridazin-3-one (<sup>18</sup>F-BCPP-BF), for quantitative imaging of MC-I in the living brain (20). A preliminary in vitro binding assay indicated that <sup>18</sup>F-BCPP-EF was more sensitive to rotenone than the others, with significantly lower nonspecific binding (16,20). In the present study, the properties of <sup>18</sup>F-BCPP-EF and <sup>18</sup>F-BCPP-BF were further evaluated regarding the affinity to MC-I using bovine cardiomyocyte submitochondrial particles (SMP), the rat whole-body kinetics by a tissue dissection method, and the effects of rotenone on MC-I binding in the rat brain and heart using small-animal PET. Furthermore, the capability of <sup>18</sup>F-BCPP-EF to detect neuronal damage was evaluated in a rat model of ischemic brain damage.

## MATERIALS AND METHODS

### Animals and Chemicals

The following experiments were approved by the Ethical Committee of the Central Research Laboratory, Hamamatsu Photonics. Male Sprague–Dawley rats (age, 8 wk; weight, 260–280 g) (Japan SLC) were used. <sup>3</sup>H-dihydrorotenone was obtained from American Radio-labeled Chemicals. Halothane and chloral hydrate were purchased from Takeda Pharmaceutical and Sigma-Aldrich, respectively. Rotenone was from MP Biochemicals LLC. Rose bengal and rabbit anti-Iba1 polyclonal antibody were from Wako Pure Chemical Industry. Mouse anti-NeuN monoclonal antibody and EnVision were obtained from Millipore and DAKO, respectively. 4,7,13,16,21,24-Hexaoxa-1,10-diazabicyclo [8,8,8]hexacosane (K[2,2,2]) was obtained from Aldrich. Mannose triflate, the precursor of <sup>18</sup>F-BMS-747158-02 (<sup>18</sup>F-BMS), and its standard compounds were obtained from NARD Institute.

### In Vitro Binding Assay

For analyses of the affinity of BCPP-EF, BCPP-BF, and BMS to MC-I, an in vitro binding assay was conducted using <sup>3</sup>H-dihydrorotenone and bovine cardiomyocyte SMP prepared according to a previous report (21). In competition experiments, the radioligand concentration was fixed at 4.5 nM, and variable concentrations of each testing compound solved in dimethyl sulfoxide were added to test tubes containing SMP (45 µg/mL protein) and incubated at 22°C for 30 min. After the incubation, the solutions were filtrated through filter papers (GF/C; Whatman) using a cell harvester (M-30R; Brandel) and washed 3 times with 50 mM Tris/HCl buffer solution (pH 7.4), and then protein-bound radioactivities remaining in the filter papers were measured using a liquid scintillation counter (3100; PerkinElmer). Specific binding was plotted against the concentration of each testing compound to determine the 50% inhibition values, which were converted to the inhibition constant (K<sub>i</sub>) using the Cheng and Prusoff equation (22).

### PET Ligand Syntheses

<sup>18</sup>F was produced by <sup>18</sup>O(p, n)<sup>18</sup>F nuclear reaction using the cyclotron (HM-18; Sumitomo Heavy Industry, Osaka, Japan) at Hamamatsu Photonics PET center. Labeled compounds were synthesized using a modified CUPID system (Sumitomo Heavy Industry). High-performance liquid chromatography (HPLC) analyses of labeled compounds were performed on a GL-7400 low-pressure-gradient HPLC system (GL Sciences, Inc.) with a radioactivity detector (RLC-700; Hitachi Aloka Medical, Inc.).

<sup>18</sup>F-BCPP-EF and <sup>18</sup>F-BCPP-BF were radiolabeled as reported previously (Supplemental Fig. 1; supplemental materials are available at <http://jnm.snmjournals.org>) (20). Radioactivity yields, radiochemical

yields, radiochemical purities, and specific radioactivities of <sup>18</sup>F-BCPP-EF and <sup>18</sup>F-BCPP-BF were 5.1 ± 0.9 and 3.7 ± 1.1 GBq (mean ± SD, *n* = 5), 30.8 ± 4.2 and 16.3% ± 2.7%, 99.1 ± 0.7 and 99.6% ± 0.6%, and 139.6 ± 37.0 and 111.8 ± 40.1 GBq/µmol, respectively.

<sup>18</sup>F-BMS was labeled as reported previously (17,18). Radioactivity yield, radiochemical yield, radiochemical purity, and specific radioactivity were 4.7 ± 1.0 GBq, 19.1% ± 3.7%, 99.6% ± 0.7%, and 67.2 ± 17.6 GBq/µmol, respectively.

<sup>18</sup>F-FDG was produced by nucleophilic <sup>18</sup>F-fluorination of mannose triflate after basic hydrolysis of 2-<sup>18</sup>F-fluoro-1,3,4,6-tetra-*O*-acetyl-*D*-glucose according to a method described previously (23).

### Tissue Dissection Assay

Three rats per each time point were used in this assessment. Five megabecquerels of <sup>18</sup>F-BCPP-EF, <sup>18</sup>F-BCPP-BF, or <sup>18</sup>F-BMS were injected into each rat through the tail vein. The animals were sacrificed by decapitation under chloral hydrate (400 mg/kg, intraperitoneally) anesthesia at 1, 5, 10, and 30 min after the injection; samples of blood, heart, lung, liver, kidney, spleen, muscle, bone, small intestine, large intestine, pancreas, and brain were rapidly removed; the weight and radioactivity were measured using a γ counter (1480 WIZARD, Perkin Elmer); and standardized uptake values (SUVs) were calculated.

For plasma metabolic analyses, the blood samples were obtained at 1, 5, 10, 30, and 60 min after the injection; centrifuged to separate plasma; and weighed. The radioactivity of the samples was measured, and methanol was added to plasma samples (sample/methanol = 1/1), followed by centrifugation. The obtained supernatants were developed with thin-layer chromatography plates (AL SIL G/UV; Whatman) with a mobile phase of ethyl acetate. The ratio of unmetabolized fraction was determined using a phosphoimaging plate (FLA-7000, Fuji Film) to calculate unmetabolized ratios of PET probes.

For brain metabolite analyses, the brain samples obtained at 5, 30, and 60 min after the injection were minced, supplemented with ice-cooled EtOH (2.0 mL), and homogenized (Polytron PT300; Kinematica AG) for 1 min. Aliquots of the homogenate (0.4 mL) were transferred to a tube and centrifuged. The resulting supernatants were separated and analyzed in the same manner as plasma samples.

Immunohistochemical assessments were performed with brains sampled at day 7 after ischemic insults using rabbit anti-Iba1 polyclonal antibody and mouse anti-NeuN monoclonal antibody as reported previously (12,16).

### PET Imaging

Vehicle alone or rotenone, a specific MC-I inhibitor, at a dose of 0.1 mg/kg in 10 mL of vehicle (*N,N*-dimethylformamide/polyethylene glycol 400/saline = 1/1/2), was infused to rats through the tail vein cannula for 1 h, then <sup>18</sup>F-BCPP-EF, <sup>18</sup>F-BCPP-BF, or <sup>18</sup>F-BMS was injected as a bolus for PET measurement. For PET imaging of ischemic neuronal damage, <sup>18</sup>F-BCPP-EF or <sup>18</sup>F-FDG was injected 1 (day 1) and 7 d (day 7) after the ischemic insult with photochemically induced thrombosis (PIT) as reported previously (12,16,24).

PET scans were conducted with a high-resolution small-animal PET scanner (ClairvivoPET; Shimadzu Corp. (25)) as described previously (12,16). Dynamic images and summation images of <sup>18</sup>F-BCPP-EF, <sup>18</sup>F-BCPP-BF, and <sup>18</sup>F-BMS from 10 to 30 min, and of <sup>18</sup>F-FDG from 40 to 60 min after the injection, were reconstructed, and created SUV images. Body temperature in rats was monitored to control using a heat pad during PET measurement. Because of technical limitation, physiologic vital signs could not be monitored. Regions of interest (ROIs) for rotenone effect assessment were placed on PET images in the cortex, striatum, and cerebellum with the aid of a rat brain atlas (26). In the ischemic PET studies, ROIs for the

perinfarct and infarct core areas were defined as the ischemic left hemisphere region showing 40%–60% (periinfarcted region) and less than 40% (core region), respectively, of  $^{18}\text{F}$ -BCPP-EF uptake in the corresponding intact side, and they were applied to a normal condition (16). The same ROIs were set on the intact right hemisphere of each condition.

### Statistical Analysis

Results are expressed as mean  $\pm$  SD. Comparisons between conditions were performed using paired, 2-tailed Student *t* tests. A probability level of less than 5% ( $P < 0.05$ ) was considered to indicate statistical significance.

### RESULTS

We determined 50% inhibition values of  $^{18}\text{F}$ -BCPP-EF,  $^{18}\text{F}$ -BCPP-BF, and  $^{18}\text{F}$ -BMS for MC-I to calculate their  $K_i$  values in the in vitro assay using bovine cardiomyocyte SMP and  $^3\text{H}$ -dihydrorotenone.  $^{18}\text{F}$ -BCPP-BF had the highest affinity ( $K_i = 0.70$  nM),  $^{18}\text{F}$ -BMS was intermediate (0.95 nM), and  $^{18}\text{F}$ -BCPP-EF showed the lowest affinity (2.31 nM) for MC-I of bovine cardiomyocyte (Supplemental Fig. 2).

Radiosyntheses of  $^{18}\text{F}$ -BCPP-EF,  $^{18}\text{F}$ -BCPP-BF, and  $^{18}\text{F}$ -BMS were conducted, and the biodistribution of these PET probes was determined by a tissue dissection method in rats (Fig. 1). The kinetics of these 3 probes in whole blood had a U shape, and thus the radioactivity levels decreased up to 10 min after the injection, followed by a gradual increase. Although precise mechanisms re-

main unclear, the decrease might be attributable to their release from organs with high uptake of PET probes at early times, such as the heart.  $^{18}\text{F}$ -BCPP-EF showed rapid uptake that was retained up to 30 min after injection, followed by a decline thereafter in the heart, kidney, small and large intestines, and pancreas. The liver exhibited rapid uptake and then remained constant throughout the study. In contrast, the brain, lung, spleen, and bone revealed gradual elimination just after the injection (Fig. 1A). At 60 min after the injection, the distribution of  $^{18}\text{F}$ -BCPP-EF was the highest in the heart; high in the kidney and liver; intermediate in the brain, pancreas, and small intestine; and low in the spleen, large intestine, lung, muscle, and bone (Fig. 1A).

The uptake levels of  $^{18}\text{F}$ -BCPP-BF in each organ were slightly lower than those of others. At 60 min after the injection, the distribution of  $^{18}\text{F}$ -BCPP-BF was the highest in the heart; high in the kidney; intermediate in the liver, brain, pancreas, small intestine, and bone; and low in the spleen, large intestine, lung, and muscle (Fig. 1B). The kidney, small and large intestines, pancreas, and liver showed rapid uptake of  $^{18}\text{F}$ -BCPP-BF that was retained up to 10 min after injection, followed by a decline thereafter. The lung and spleen revealed gradual elimination just after the injection. In contrast, the uptake in the heart and bone continuously increased with time after  $^{18}\text{F}$ -BCPP-BF injection (Fig. 1B).

The patterns of time–activity curves of  $^{18}\text{F}$ -BMS uptake were generally the same as those of  $^{18}\text{F}$ -BCPP-EF, except in the liver, in which the uptake of  $^{18}\text{F}$ -BMS increased up to 30 min after injection, followed by a gradual decline (Fig. 1C).

Peak values of brain-to-blood (15.5) and heart-to-blood (63.0) ratios of  $^{18}\text{F}$ -BCPP-EF were observed 10 min after the injection (Table 1), whereas the ratios of  $^{18}\text{F}$ -BCPP-BF continuously increased up to 60 min after the injection, showing 14.9 and 83.7, respectively (Table 1). These peak values of  $^{18}\text{F}$ -BCPP-EF and  $^{18}\text{F}$ -BCPP-BF were significantly higher than those of  $^{18}\text{F}$ -BMS (11.5 and 56.2, respectively, Table 1).

The metabolic analyses of  $^{18}\text{F}$ -BCPP-EF and  $^{18}\text{F}$ -BCPP-BF revealed the gradual degradation to polar metabolites at a relatively slow rate, with 17.3% and 18.4%, respectively, remaining as each parent compound 30 min after the injection (Table 2).  $^{18}\text{F}$ -BMS was metabolized more rapidly than others, showing only 7.5% at 30 min after the injection (Table 2). In contrast, the metabolic profiles of  $^{18}\text{F}$ -BCPP-EF,  $^{18}\text{F}$ -BCPP-BF, and  $^{18}\text{F}$ -BMS indicated greater stability in the brain than those in the plasma, showing 90.5%, 97.1%, and 87.2%, respectively, 30 min after the injection (Table 2).

Small-animal PET imaging of rats with  $^{18}\text{F}$ -BCPP-EF,  $^{18}\text{F}$ -BCPP-BF, and  $^{18}\text{F}$ -BMS revealed high uptake into the brain (SUV = 2.9, 2.0, and 3.0, respectively) (Figs. 2 and 3) and heart (SUV = 10.2, 8.6, and 10.6, respectively, at 30 min after

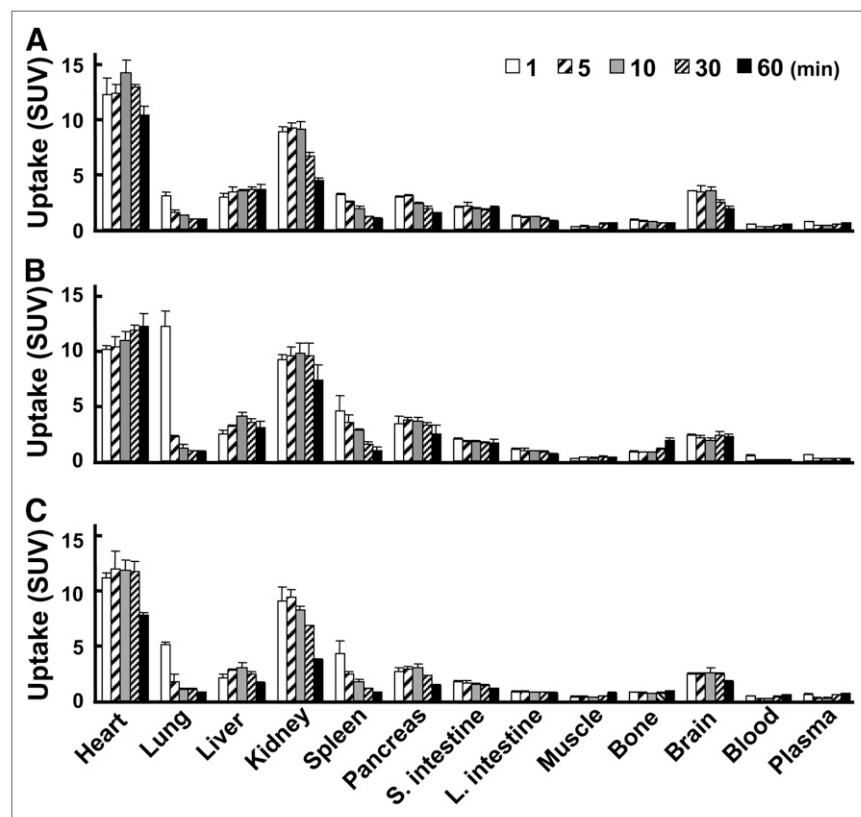


**FIGURE 1.** Distribution and kinetics of  $^{18}\text{F}$ -BCPP-EF (A),  $^{18}\text{F}$ -BCPP-BF (B), and  $^{18}\text{F}$ -BMS (C) in rats. Rats were intravenously injected with 5 MBq of  $^{18}\text{F}$ -BCPP-EF,  $^{18}\text{F}$ -BCPP-BF, or  $^{18}\text{F}$ -BMS via tail vein and sacrificed 1, 5, 10, 30, and 60 min after injection to calculate SUV. All values are expressed as mean  $\pm$  SD for 3 animals.

**TABLE 1**  
Uptake Ratios of Brain to Blood, Brain to Plasma, Heart to Blood, and Heart to Plasma of <sup>18</sup>F-BCPP-EF, <sup>18</sup>F-BCPP-BF, and <sup>18</sup>F-BMS in Rat

Probe	1 min	5 min	10 min	30 min	60 min
<b><sup>18</sup>F-BCPP-EF</b>					
Brain to blood	7.643 ± 0.495	15.058 ± 1.358	15.525 ± 2.178	7.866 ± 0.453	4.411 ± 0.435
Brain to plasma	5.280 ± 0.217	11.703 ± 1.361	11.879 ± 1.559	5.941 ± 0.502	3.328 ± 0.642
Heart to blood	26.785 ± 1.387	54.629 ± 3.596	63.098 ± 6.226	41.310 ± 4.125	24.705 ± 1.546
Heart to plasma	18.554 ± 1.699	40.049 ± 1.853	48.291 ± 4.328	31.229 ± 3.950	18.638 ± 1.245
<b><sup>18</sup>F-BCPP-BF</b>					
Brain to blood	4.432 ± 0.371	13.362 ± 1.321	12.567 ± 0.708	14.817 ± 3.156	14.978 ± 3.006
Brain to plasma	3.926 ± 0.319	10.986 ± 1.042	10.039 ± 0.786	11.658 ± 2.918	11.112 ± 2.304
Heart to blood	19.617 ± 0.680	65.826 ± 5.418	72.429 ± 1.703	76.204 ± 3.909	83.791 ± 18.636
Heart to plasma	17.391 ± 1.020	54.127 ± 4.272	57.818 ± 2.271	59.739 ± 5.148	62.153 ± 14.094
<b><sup>18</sup>F-BMS</b>					
Brain to blood	5.483 ± 1.289	11.318 ± 1.328	11.568 ± 2.916	6.141 ± 0.399	3.169 ± 0.124
Brain to plasma	4.291 ± 1.030	8.804 ± 1.116	9.039 ± 2.329	4.657 ± 0.128	2.511 ± 0.119
Heart to blood	25.195 ± 4.438	56.286 ± 5.319	53.204 ± 8.714	29.393 ± 2.996	14.379 ± 0.442
Heart to plasma	19.720 ± 3.658	43.831 ± 5.400	41.555 ± 6.982	22.268 ± 1.422	11.385 ± 0.172

Rats were intravenously injected with 5 MBq of <sup>18</sup>F-BCPP-EF, <sup>18</sup>F-BCPP-BF, or <sup>18</sup>F-BMS via tail vein and sacrificed at 1, 5, 10, 30, and 60 min after injection to obtain tissue samples for uptake ratio analyses. All values are expressed as mean ± SD for 3 animals.

injection) (Figs. 2 and 4). Under the vehicle condition, the radioactivity level of <sup>18</sup>F-BCPP-EF in the brain showed rapid uptake and gradual decrease with time just after the injection (Fig. 3A), whereas <sup>18</sup>F-BCPP-BF remained constant throughout the PET measurements up to 60 min after the injection (Fig. 3B). <sup>18</sup>F-BMS remained constant for 30 min after the injection, followed by gradual reduction (Fig. 3C). In the heart, <sup>18</sup>F-BCPP-EF exhibited slow accumulation up to 30 min after the injection, followed by slight washout (Fig. 4A), whereas <sup>18</sup>F-BCPP-BF constantly increased up to 60 min after the injection (Fig. 4B). <sup>18</sup>F-BMS exhibited slow accumulation, followed by its maintenance at a constant level at 20 min and later (Fig. 4C). With preadministration of rotenone (0.1 mg/kg/h), the uptake levels of <sup>18</sup>F-BCPP-EF and <sup>18</sup>F-BMS into the brain showed a significant reduction, and the degree of reduction of <sup>18</sup>F-BCPP-EF (Figs. 2A and 3A) was much more pronounced than that of <sup>18</sup>F-BMS (Figs. 2C and 3C, lower). In the heart, rotenone administration

induced reduction of <sup>18</sup>F-BCPP-EF (Figs. 2A and 4A) and <sup>18</sup>F-BMS uptake (Figs. 2C and 3C), with faster elimination rates than in the vehicle condition. No significant reduction of <sup>18</sup>F-BCPP-BF uptake was observed in either brain or heart (Figs. 2B, 3B, and 4B). The SUVs of <sup>18</sup>F-BCPP-EF and <sup>18</sup>F-BMS, assessed 30 min after the injection, were suppressed by the preadministration of rotenone (0.1 mg/kg) to 65.4% and 85.6% of the vehicle condition in the brain (Figs. 3A and 3C) and 53.7% and 81.7% of the vehicle condition in the heart, respectively (Figs. 4A and 4C).

At day 1 after ischemic insult, PIT induced a decrease in the uptake of <sup>18</sup>F-FDG (Fig. 5, left, and Fig. 6, left) in the infarct region of the left ischemic hemisphere; however, there was higher uptake in the ischemic region than in the corresponding region in the intact side at day 7 (Fig. 5, left, and Fig. 6, left), which overlapped with high immunoreactivity to anti-Iba 1 antibody (Fig. 7, upper). In contrast, PET imaging with <sup>18</sup>F-BCPP-EF demonstrated a significant reduction in the infarct region of the left ischemic

**TABLE 2**  
Metabolic Profiles of <sup>18</sup>F-BCPP-EF, <sup>18</sup>F-BCPP-BF, and <sup>18</sup>F-BMS in Rat Brain and Plasma

Probe	1 min	5 min	10 min	30 min	60 min
<b><sup>18</sup>F-BCPP-EF</b>					
Brain	ND	98.5 ± 0.1	ND	90.5 ± 0.2	84.4 ± 0.1
Plasma	84.5 ± 3.2	46.1 ± 8.0	40.4 ± 4.8	17.3 ± 2.6	8.3 ± 0.9
<b><sup>18</sup>F-BCPP-BF</b>					
Brain	ND	99.3 ± 0.1	ND	97.1 ± 0.1	95.3 ± 0.1
Plasma	92.5 ± 0.3	69.5 ± 1.6	39.8 ± 2.0	18.4 ± 3.5	12.1 ± 3.6
<b><sup>18</sup>F-BMS</b>					
Brain	ND	97.9 ± 0.3	ND	87.2 ± 0.5	76.3 ± 1.2
Plasma	89.8 ± 1.5	39.9 ± 3.5	24.3 ± 9.3	7.5 ± 1.8	2.9 ± 0.7

Rats were intravenously injected with 5 MBq of <sup>18</sup>F-BCPP-EF, <sup>18</sup>F-BCPP-BF, or <sup>18</sup>F-BMS via tail vein and sacrificed at 1, 5, 10, 30, and 60 min after injection to obtain brain and plasma for metabolic analyses. All values are expressed as mean ± SD for 3 animals. ND = not determined.

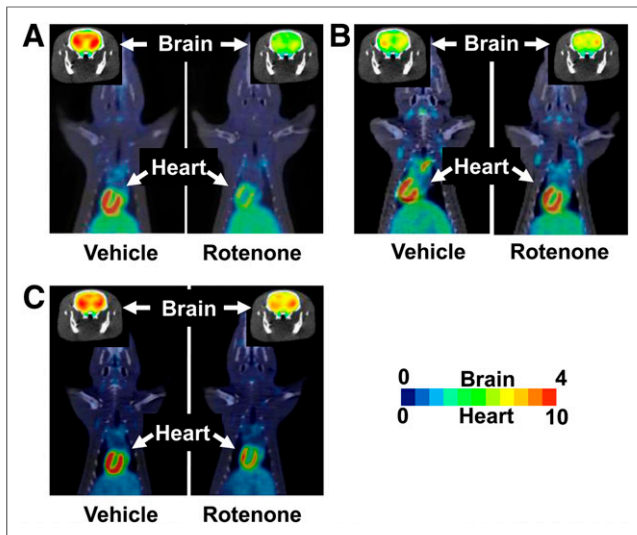


**FIGURE 2.** Effects of preadministration of rotenone on uptake of  $^{18}\text{F}$ -BCPP-EF (A),  $^{18}\text{F}$ -BCPP-BF (B), and  $^{18}\text{F}$ -BMS (C) in rats imaged by small-animal PET and X-CT. After continuous infusion of vehicle or rotenone at dose of 0.1 mg/kg/h for 1 h, PET scanning was conducted for 60 min after injection of each PET probe. Summation PET data from 10 to 30 min for A, B, and C were reconstructed for SUV images, and then PET images were superimposed on individual X-CT images.

hemisphere from day 1 and later after the ischemic insult induced by PIT (Fig. 5, right, and Fig. 6, right). At day 1, the damaged areas determined by  $^{18}\text{F}$ -BCPP-EF as core regions were well correlated with those measured by 2,3,5-triphenyltetrazolium chloride staining (Supplemental Fig. 3). At day 7, the low uptake area determined with  $^{18}\text{F}$ -BCPP-EF (Fig. 5, right) corresponded to the area with low immunoreactivity to anti-NeuN antibody (Fig. 7, lower).

## DISCUSSION

The present study evaluated the capability of  $^{18}\text{F}$ -BCPP-EF and  $^{18}\text{F}$ -BCPP-BF (20) as PET probes for imaging the MC-I activity in the living rat brain in comparison with a previously reported probe  $^{18}\text{F}$ -BMS (17,18).

The accumulation of  $^{18}\text{F}$ -BMS was reported to depend on cellular MC-I activity, which is the first component of 4 electron transport complexes in the inner mitochondrial membrane (17,18). By an *in vitro* assay in a monolayer of neonatal rat cardiomyocytes, it was confirmed that  $^{18}\text{F}$ -BMS uptake was inhibited by rotenone, a specific MC-I inhibitor (17).  $^{18}\text{F}$ -BMS was also expected to show uptake in the brain because of the high density of mitochondria, not only in the heart but also in the brain. Our previous results demonstrated that  $^{18}\text{F}$ -BMS might be a useful PET probe to detect the ischemic damages of MC-I not only at the acute but also at the subacute phase, at which time the remarkable microglial activation in the ischemic damaged area was determined by PET with  $^{11}\text{C}$ -(R)-PK11195 and  $^{18}\text{F}$ -FDG as well as immunohistochemical analysis with anti-Iba1 antibody (12,16). Because activated inflammatory cells (macrophages and microglia) exclusively produce ATP through the enhanced glycolysis with a low contribution of the electron transport system including MC-I for ATP production, these cells need more glucose to survive and also uptake more  $^{18}\text{F}$ -FDG than normal neuronal and

glial tissues. These metabolic properties resulted in the apparently high uptake of  $^{18}\text{F}$ -FDG in damaged areas in which activated inflammatory cells accumulated (12,16). To measure the viability of neuronal and glial tissues by PET and to avoid underestimation of damaged areas as observed by  $^{18}\text{F}$ -FDG, PET targeting mitochondrial function was expected to be useful (8,16).

*In vitro* assessment with living brain slices and *in vivo* assessment using small-animal PET suggested that  $^{18}\text{F}$ -BMS has relatively high nonspecific binding in brain tissues against inhibition with rotenone (16). Therefore, we tried to modify the chemical structure of  $^{18}\text{F}$ -BMS to induce lower lipophilicity (20). As reported previously, the lipophilicity indices of  $\log D_{7.4}$  were 3.03, 4.27, and 3.69 for  $^{18}\text{F}$ -BCPP-EF,  $^{18}\text{F}$ -BCPP-BF, and  $^{18}\text{F}$ -BMS, respectively (20), which are within the appropriate range of  $\log D_{7.4}$  for blood-brain barrier penetration (19). It was expected that, if the brain uptake was exclusively lipophilicity-driven, the rank order of brain uptake should have been high in  $^{18}\text{F}$ -BCPP-BF, intermediate in  $^{18}\text{F}$ -BMS, and low in  $^{18}\text{F}$ -BCPP-EF. However, the assessed results indicated that  $^{18}\text{F}$ -BCPP-BF with the highest lipophilicity showed the lowest brain uptake. The prospected transport mechanisms of these compounds need to take into account more complex systems.

The specificity of  $^{18}\text{F}$ -BCPP-EF binding to MC-I was confirmed by preadministration of rotenone. Although a dose-escalation

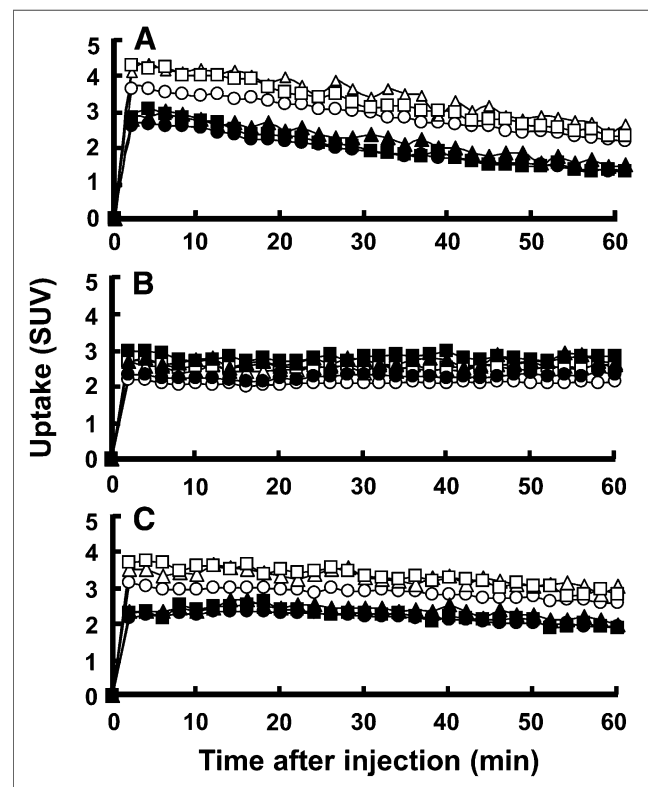


**FIGURE 3.** Effects of preadministration of rotenone on time-activity curves of  $^{18}\text{F}$ -BCPP-EF (A),  $^{18}\text{F}$ -BCPP-BF (B), and  $^{18}\text{F}$ -BMS (C) in rat brain. PET scans were conducted as described in Figure 2, and then summation data from 10 to 30 min were reconstructed for SUV images. ROIs for brain were set on reconstructed PET images to obtain time-activity curves of each PET probe in these regions.  $\circ$  = cortex-vehicle;  $\bullet$  = cortex-rottenone;  $\triangle$  = striatum-vehicle;  $\blacktriangle$  = striatum-rottenone;  $\square$  = cerebellum-vehicle;  $\blacksquare$  = cerebellum-rottenone.

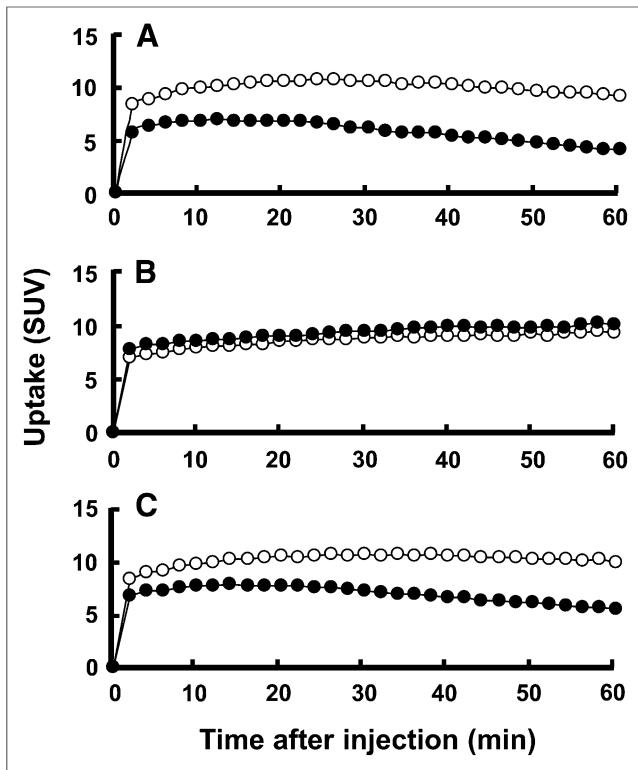


**FIGURE 4.** Effects of preadministration of rotenone on time-activity curves of  $^{18}\text{F}$ -BCPP-EF (A),  $^{18}\text{F}$ -BCPP-BF (B), and  $^{18}\text{F}$ -BMS (C) in rat heart. PET scans were conducted as described in Figure 2, and then summation data from 10 to 30 min were reconstructed for SUV images. ROIs for heart (myocardium) were set on reconstructed PET images to obtain time-activity curves of each PET probe in these regions.  $\circ$  = vehicle;  $\bullet$  = rotenone.

study was impossible because of its lethal effects on the cardiac function, a significant reduction of uptake of  $^{18}\text{F}$ -BCPP-EF and  $^{18}\text{F}$ -BMS was observed in the brain and heart, even at a relatively low dose of 0.1 mg/kg/h. In contrast, preadministration of

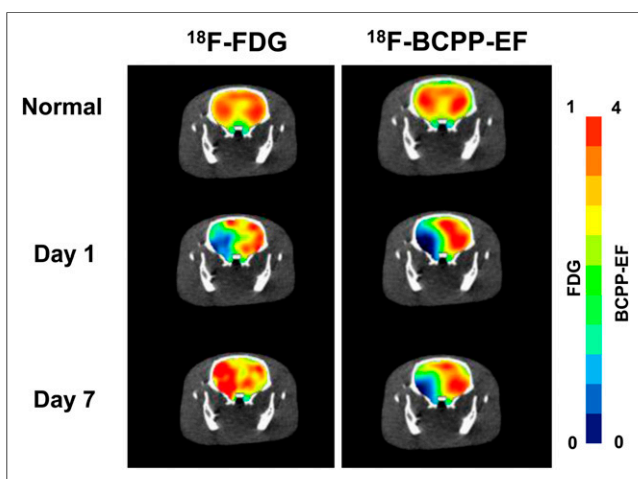


**FIGURE 5.** Temporal changes in PET images of  $^{18}\text{F}$ -FDG and  $^{18}\text{F}$ -BCPP-EF in rat brains of PIT model. PET scans were conducted for 60 min with each PET probe before (normal), 1 (day 1), and 7 d (day 7) after PIT operation.

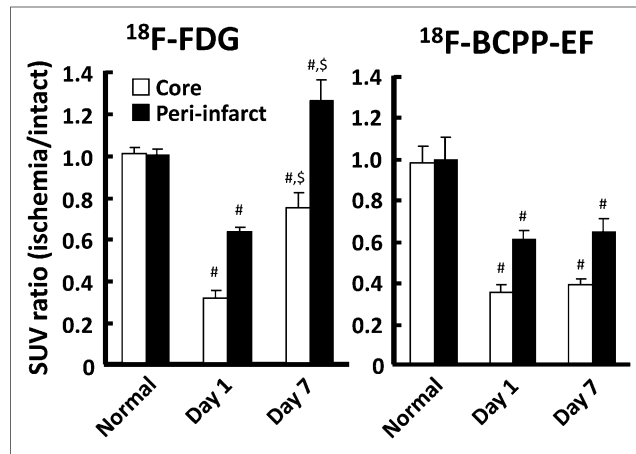


**FIGURE 6.** Temporal changes in uptake (SUV ratio) of  $^{18}\text{F}$ -FDG and  $^{18}\text{F}$ -BCPP-EF in rat brains of PIT model. PET scans were conducted for 60 min with each PET probe before (normal), 1 (day 1), and 7 d (day 7) after PIT operation. # $P < 0.01$  vs. corresponding normal condition. \$ $P < 0.01$  vs. corresponding day 1 condition.

rotenone induced no significant reduction of  $^{18}\text{F}$ -BCPP-BF in both brain and heart, because of its high  $K_i$  value to MC-I determined using SMP and  $^3\text{H}$ -dihydrorotenone. The high affinity of  $^{18}\text{F}$ -BCPP-BF to MC-I was also suggested by its nonreversible (brain) and accumulated-type kinetics (heart) in rat using animal PET imaging, the kinetics of which are not always suitable for quantitative imaging analysis of brain function using PET (27,28).

For  $^{18}\text{F}$ -labeled PET probes,  $^{18}\text{F}$ -BCPP-EF indicated minimal defluorination in plasma. In contrast,  $^{18}\text{F}$ -BCPP-BF exhibited the increasing accumulation of radioactivity in bone with time after the injection, suggesting the instability with defluorination. It was reported to be a common mechanism of  $^{18}\text{F}$ -fluoride formation that P-450-mediated hydroxylation occurred at  $^{18}\text{F}$ -fluorine-substituted carbon, followed by spontaneous elimination (29,30). In contrast, the substitution of oxygen at  $\beta$  carbon decreased the reactivity toward hydroxylation, leading to slower  $^{18}\text{F}$ -fluoride release (31). Thus, the differences of metabolic stability among these PET probes against P-450-mediated hydroxylation could be considered attributable to the chemical structural differences.

$^{18}\text{F}$ -BCPP-EF could detect impaired MC-I activity in the living brains of the ischemic rat model, revealing the lower uptake of  $^{18}\text{F}$ -BCPP-EF in the ischemia-damaged area than intact area. As observed at day 7,  $^{18}\text{F}$ -FDG showed high uptake in the ischemia-damaged region, in which  $^{18}\text{F}$ -BCPP-EF revealed low uptake. These results strongly suggested that this reduction was related to MC-I specific binding, not to a simply reduced delivery by ischemic insult. The reactive oxygen species (ROS) play a role in cell injury associated with cortical ischemia and reperfusion. The PIT model has been considered as the most relevant to the pathologic cascade occurring after clinical infarction among the experimental ischemic rodent models (24). Thus, the reperfusion-injurylike phenomenon, occurring after clinical infarction, could be involved in the progress of more severe brain damage than a permanent occlusion model (32,33), suggesting that reperfusion-related ROS production may in part contribute to neuronal damage of reperfusion injury. Mitochondria are considered the main intracellular source of ROS and also the main target of

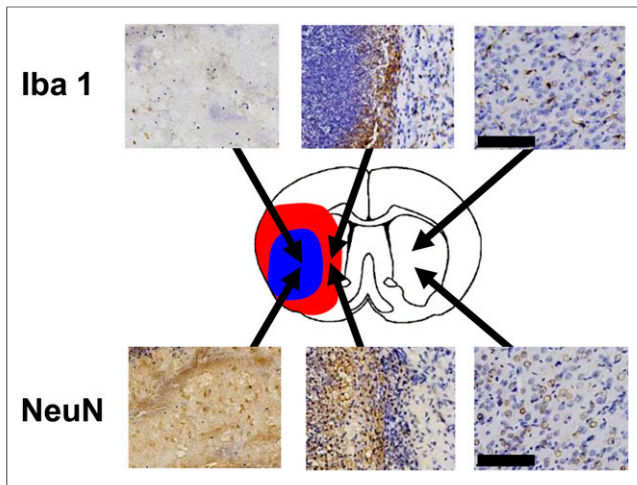


**FIGURE 7.** Immunohistochemical analyses in rat brains of PIT model. Brains were dissected at day 7 for immunohistochemistry with Iba1 for inflammation and NeuN for neurons.

oxyradical-mediated damage. When ischemic tissue is reoxygenated, electron transport through the respiratory chain is impaired because of depletion of adenosine diphosphate during ischemia, and this leads to a burst of ROS generation during the first minutes of reoxygenation (34). Because MC-I exhibits lower activity than the other respiratory chain complexes, it is considered a limiting factor in the regulation of oxidative phosphorylation (35). Taking these findings together, PET imaging with  $^{18}\text{F}$ -BCPP-EF, which has specificity for MC-I activity and which was not affected by the inflammation with microglial activation, could be expected to provide more accurate information about neurodegenerative damage than  $^{18}\text{F}$ -FDG.

One of the limitations of this study might be applying SUV analysis for  $^{18}\text{F}$ -BCPP-EF binding to MC-I. Because total volume of blood was small in rats, kinetic analyses using the metabolite-corrected plasma input function were difficult for full quantitative analysis. However, we preliminarily conducted the correlation analysis between SUV (averaged between 40 and 60 min after injection) and 2-tissue-compartment model analyses (total distribution volume [ $V_T$ ]) using the metabolite-corrected plasma input function in conscious monkeys. As a result, SUV and  $V_T$  showed good correlation with, an  $R^2$  of 0.625 and a  $P$  value less than 0.001, suggesting that SUV analysis used in the present study could be applicable for semiquantitative analysis for  $^{18}\text{F}$ -BCPP-EF binding to MC-I (Tsukada et al., unpublished data, 2013).

## CONCLUSION

The present preliminary results demonstrated that  $^{18}\text{F}$ -BCPP-EF has the capability to detect neuronal degeneration as impaired MC-I activity in the living rat brains of an ischemic brain model.

## DISCLOSURE

The costs of publication of this article were defrayed in part by the payment of page charges. Therefore, and solely to indicate fact, this article is hereby marked "advertisement" in accordance with 18 USC section 1734. No potential conflict of interest relevant to this article was reported.

## ACKNOWLEDGMENTS

We gratefully acknowledge the technical assistance provided by Takeharu Kakiuchi, Shigeyuki Yamamoto, Yuko Kato, and Teruyo Hosoya.

## REFERENCES

- Boyle PJ, Scott JC, Krentz AJ, et al. Diminished brain glucose metabolism is a significant determinant for falling rates of systemic glucose utilization during sleep in normal humans. *J Clin Invest.* 1994;93:529–535.
- Powers WJ, Videen TO, Markham J, et al. Selective defect of in vivo glycolysis in early Huntington's disease striatum. *Proc Natl Acad Sci USA.* 2007;104:2945–2949.
- Vander Heiden MG, Cantley LC, Thompson CB. Understanding the Warburg effect: the metabolic requirements of cell proliferation. *Science.* 2009;324:1029–1033.
- Radu CG, Shu CJ, Shelly SM, Phelps ME, Witte ON. Positron emission tomography with computed tomography imaging of neuroinflammation in experimental autoimmune encephalomyelitis. *Proc Natl Acad Sci USA.* 2007;104:1937–1942.
- Maciver NJ, Jacobs SR, Wieman HL, et al. Glucose metabolism in lymphocytes is a regulated process with significant effects on immune cell function and survival. *J Leukoc Biol.* 2008;84:949–957.
- Garedew A, Henderson SO, Moncada S. Activated macrophages utilize glycolytic ATP to maintain mitochondrial membrane potential and prevent apoptotic cell death. *Cell Death Differ.* 2010;17:1540–1550.
- Rodríguez-Prados JC, Través PG, Cuenca J, et al. Substrate fate in activated macrophages: a comparison between innate, classic, and alternative activation. *J Immunol.* 2010;185:605–614.
- Warburg O. On respiratory impairment in cancer cells. *Science.* 1956;124:269–270.
- Koppenol WH, Bounds PL, Dang CV. Otto Warburg's contributions to current concepts of cancer metabolism. *Nat Rev Cancer.* 2011;11:325–337.
- Chugani HT, Phelps ME, Mazziotta JC. Positron emission tomography study of human brain functional development. *Ann Neurol.* 1987;22:487–497.
- Schroeter M, Dennin MA, Walberer M, et al. Neuroinflammation extends brain tissue at risk to vital peri-infarct tissue: a double tracer [ $^{11}\text{C}$ ]PK11195- and [ $^{18}\text{F}$ ]FDG-PET study. *J Cereb Blood Flow Metab.* 2009;29:1216–1225.
- Fukumoto D, Hosoya T, Nishiyama S, et al. Multiparametric assessment of acute and sub-acute ischemic neuronal damage: a small animal PET study with rat photochemically induced thrombosis (PIT) model. *Synapse.* 2011;65:207–214.
- Winkler A, Boisgard R, Martin A, Tavitian B. Radioisotopic imaging of neuroinflammation. *J Nucl Med.* 2010;51:1–4.
- Jacobs AH, Tavitian B, INMiND consortium. Noninvasive molecular imaging of neuroinflammation. *J Cereb Blood Flow Metab.* 2012;32:1393–1415.
- Suzuki K, Sugihara G, Ouchi Y, et al. Microglial activation in young adults with autism spectrum disorder. *JAMA Psychiatry.* 2013;70:49–58.
- Fukumoto D, Nishiyama S, Harada N, Yamamoto S, Tsukada H. Detection of ischemic neuronal damage with [ $^{18}\text{F}$ ]BMS-747158-02, a mitochondrial complex-1 PET ligand: small animal PET study in rat brain. *Synapse.* 2012;66:909–917.
- Yalamanchili P, Wexler E, Hayes M, et al. Mechanism of uptake and retention of F-18 BMS-747158-02 in cardiomyocytes: a novel PET myocardial imaging agent. *J Nucl Cardiol.* 2007;14:782–788.
- Huisman MC, Higuchi T, Reder S, et al. Initial characterization of an  $^{18}\text{F}$ -labeled myocardial perfusion tracer. *J Nucl Med.* 2008;49:630–636.
- Waterhouse RN. Determination of lipophilicity and its use as a predictor of blood-brain barrier penetration of molecular imaging agents. *Mol Imaging Biol.* 2003;5:376–389.
- Harada N, Nishiyama S, Kanazawa M, Tsukada H. Development of novel PET probes, [ $^{18}\text{F}$ ]BCPP-EF, [ $^{18}\text{F}$ ]BCPP-BF, and [ $^{11}\text{C}$ ]BCPP-EM for mitochondrial complex 1 imaging. *J Labelled Comp Radiopharm.* 2013;56:553–561.
- Okun JG, Lummen P, Brandt U. Three classes of inhibitors share a common binding domain in mitochondrial complex I (NADH:ubiquinone oxidoreductase). *J Biol Chem.* 1999;274:2625–2630.
- Cheng Y, Prusoff WH. Relationship between the inhibition constant ( $K_i$ ) and the concentration of inhibitor which causes 50 percent inhibition ( $\text{IC}_{50}$ ) of an enzymatic reaction. *Biochem Pharmacol.* 1973;22:3099–3108.
- Oberdorfer F, Hull WE, Traving BC, Maier-Borst W. Synthesis and purification of 2-deoxy-2- $^{18}\text{F}$ -fluoro-D-glucose and 2-deoxy-2- $^{18}\text{F}$ -fluoro-D-mannose: characterization of products by  $^1\text{H}$  and  $^{19}\text{F}$ -NMR spectroscopy. *Int J Appl Radiat Isot.* 1986;37:695–701.

24. Umemura K, Wada K, Uematsu T, Nakashima M. Evaluation of the combination of a tissue-type plasminogen activator, SUN9216, and a thromboxane A2 receptor antagonist, vaproprost, in a rat middle cerebral artery thrombosis model. *Stroke*. 1993;24:1077–1081.
25. Mizuta T, Kitamura K, Iwata H, et al. Performance evaluation of a high-sensitivity large-aperture small-animal PET scanner: ClairvivoPET. *Ann Nucl Med*. 2008;22:447–455.
26. Paxinos G, Watson C. *The Rat Brain in Stereotaxic Coordinates*. 6th ed. San Diego, CA: Elsevier; 2007.
27. Koeppel RA, Frey KA, Mulholland GK, et al. [<sup>11</sup>C]Tropanyl benzilate binding to muscarinic cholinergic receptors: methodology and kinetic modeling alterations. *J Cereb Blood Flow Metab*. 1994;14:85–99.
28. Farde L, Eriksson L, Blomqvist G, Halldin C. Kinetic analysis of central [<sup>11</sup>C]raclopride binding to D<sub>2</sub>-dopamine receptors studied by PET: a comparison to the equilibrium analysis. *J Cereb Blood Flow Metab*. 1989;9:696–708.
29. Anders MW, Pohl LR. Halogenated alkanes. In: Anders MW, ed. *Bioactivation of Foreign Compounds*. New York, NY: Academic Press, 1985:283–313.
30. DeGrado TR, Moka DC. Non- $\beta$ -oxidizable  $\omega$ -[<sup>18</sup>F]fluoro long chain fatty acid analogs show cytochrome P-450-mediated defluorination: implications for the design of PET tracers of myocardial fatty acid utilization. *Int J Rad Appl Instrum B*. 1992;19:389–397.
31. French A, Napolitano E, VanBroeklin H, et al. The  $\beta$ -heteroatom effect in metabolic defluorination: the interaction of resonance and inductive effects may be a fundamental determinant in the metabolic liability of fluorine-substituted compounds. *J Labelled Comp Radiopharm*. 1991;30:431–433.
32. Takamatsu H, Tsukada H, Kakiuchi T, et al. Changes in local cerebral blood flow in photochemically induced thrombotic occlusion model in rats. *Eur J Pharmacol*. 2000;398:375–379.
33. Tsukada H, Fukumoto D, Nishiyama S, et al. Transient focal ischemia affects the cAMP second messenger system and coupled dopamine D<sub>1</sub> and 5-HT<sub>1A</sub> receptors in the living monkey brain: a PET study using microdialysis. *J Cereb Blood Flow Metab*. 2004;24:898–906.
34. Zweier JL, Flaherty JT, Weisfeldt ML. Direct measurement of free radical generation following reperfusion of ischemic myocardium. *Proc Natl Acad Sci USA*. 1987;84:1404–1407.
35. Cadenas E, Boveris A, Ragan CI, Stoppani AOM. Production of superoxide radicals and hydrogen peroxide by NADH-ubiquinone reductase and ubiquinol-cytochrome *c* reductase from beef-heart mitochondria. *Arch Biochem Biophys*. 1977;180:248–257.